Density functional simulations of a conductive bridging random access memory cell: Ag filament formation in amorphous GeS_2

Jaakko Akola*
Department of Physics, Norwegian University of Science and Technology (NTNU), NO-7491 Trondheim, Norway and Computational Physics Laboratory, Tampere University, FI-33101 Tampere, Finland

Konstantinos Konstantinou
Computational Physics Laboratory, Tampere University, FI-33101 Tampere, Finland

R. O. Jones
Peter Grünberg Institut PGI-1 and JARA/HPC, Forschungszentrum Jülich, D-52425 Jülich, Germany

(Received 13 December 2021; accepted 16 February 2022; published 4 March 2022)

Density functional/molecular dynamics simulations have been performed to shed light on the drift of Ag atoms in an amorphous GeS_2 solid-state electrolyte between Ag and Pt electrodes in the presence of a finite electric field. The system models a conductive bridging random access memory device, where the electric field induces the formation of conductive filaments across the chalcogenide. Simulations of a 1019-atom structure under an external electrostatic potential of 0.20 eV/Å at 480 and 680 K show significant atomic diffusion within 500 ps. Ag migration and the formation of percolating filaments occur in both cases. Three simulations for a smaller model (472 atoms) confirm the formation of percolating Ag strings. Significantly reduced mobility of Ag cations at 380 K means that Ag migration to the Pt electrode did not occur within 1 ns. The electronic structure analysis of selected snapshots shows that dissolved Ag atoms become markedly cationic, which changes when Ag clusters form at the Pt electrode. The electrolyte does not conduct, despite percolating single-atom Ag wire segments. Sulfur becomes anionic during the migration as a result of Ag-S bonding, and the effect is most pronounced near the active electrode. The formation of conductive filaments requires a percolating network of Ag clusters to grow from the Pt interface, and the weakest link of this network is at the Ag electrode.

DOI: 10.1103/PhysRevMaterials.6.035001

I. INTRODUCTION

The explosive increase in memory demands in computing is by no means a recent development, and replacements for magnetic hard disk drives and flash memory have been sought for many years. The need for highly scalable, rapid, low-power and durable, non-volatile alternatives has focused on a range of devices often referred to as resistive random access memories (RRAMs or ReRAM). Information is stored as states of different resistivity that can be monitored by appropriate physical mechanisms, and well-known examples are phase change memory (PCM) materials. These are based on the extremely rapid and reversible transformations between the amorphous and crystalline forms of nanosized bits in a very thin polycrystalline layer of a narrow-gap semiconductor or semimetal. Phase changes are achieved by laser light or resistive heating and can be monitored by changes in optical properties or resistivity [1]. The best-studied PCM materials are alloys of the GST family $(GeTe)_{1-x}(Sb_2Te_3)_x$, particularly $Ge_2Sb_2Te_5$, and Sb-rich compounds, including Ag/In/Sb/Te alloys. The past decade has seen much progress in understanding the phase change mechanism, and molecular dynamics (MD) simulations based on density functional (DF) theory have played an essential role.

Other candidates for nonvolatile memory are based on a metal-insulator-metal electrochemical cell [2,3], where resistance change accompanies the formation or removal of filaments in the electrolyte, depending on the polarity of the electrodes. Two promising examples are valence change memory (also known as oxygen vacancy RAM, OxRAM [3]) and conductive bridging RAM (CBRAM). The switching mechanism in the former is based on the creation and displacement of oxygen vacancies in an insulating layer that often comprises a transition metal oxide such as HfO_x [4,5], where the valence of the metal ion changes on switching. The active anode in CBRAM is often Ag or Cu, the inert cathode W or Pt [6], and common electrolytes are amorphous Ge chalcogenides, particularly Ge/S [7], and SiO_x [8–11]. Information is stored via resistivity changes caused by oxidation of an Ag or Cu metal at the anode and the reduction of Ag^+ or Cu^+ at the cathode. The low applied bias (several hundred mV) can change the resistance by many orders of magnitude in tens of nanoseconds, and a reverse bias of the same magnitude reverses the process. Flash memory uses charge in a capacitor to store information, which is retained in CBRAM as electrodeposited metal atoms with much higher stability. CBRAM is the focus of the present work.

*jaakko.akola@ntnu.no

The complex processes occurring during the operation of RRAM cells are typical of the general problem of atomic diffusion in amorphous materials, and aspects of filament formation remain poorly understood and matters of debate [4]. The resolution of such questions will require insight into the motion of individual atoms, and numerical simulations will play a central role [4,12, and references therein]. Essential input is a prescription for determining the energies and forces in a mobile, disordered system, and MD simulations of $Cu/SiO_2/Cu$ CBRAM cells have been carried out using an interatomic potential (ReaxFF) [8]. The effect of an electric field was incorporated by modifying the electronegativities of the atoms in the electrodes as the simulation proceeds. It was found that stable metallic clusters can form *before* filaments, which often lack crystalline order. Recent developments in machine learning methods of optimizing force fields promise reliable results for longer simulations of larger samples [13, and references therein].

Density functional calculations [14] are free of adjustable parameters, and their combination with MD has provided encouraging results in earlier work on related chalcogenide materials, including experimentally constrained structures of AsS_2 and $AgAsS_2$ [15] and Ag/Ge/S alloys [16]. The high mobility of Ag ions in these electrolytes is related to the presence of cavities (vacancies) and the possibility of Ag jumps to a neighboring vacant site. DF/MD simulations have been carried out for $Cu/SiO_2/Cu$ cells, although calculations of the dynamical matrix used forces calculated using ReaxFF parameters chosen to model the switching behavior of CBRAM cells [4]. The combination of DF calculations with calculations of transport coefficients [4] using non-equilibrium Green's functions [17] is desirable, but difficult to implement because of the numerical demands of DF calculations [4].

DF calculations often assume periodic boundary conditions, and the scalar potential of a *finite* electric field is neither periodic nor bounded from below. These problems can be overcome, in principle, by using the Berry phase approach [18,19], but numerical instabilities complicate their practical implementation. The limits on the simulation depend on the band gap in the material, the magnitude of the field, and the size of the simulation cell. If the field is too high, the sample too large, or the gap too small, the electronic calculation will not converge. For example, a recent study [20] applied the Berry phase approach with hybrid DFT to ascertain their effect on the midgap electronic states in models of the prototypical amorphous phase-change memory material, $Ge_2Sb_2Te_5$. It was concluded that a field stronger than 0.005 V/Å could not be used in MD simulations for this system (cubic cell 22 Å, band gap ∼0.6 eV).

We describe here DF/MD simulations of Ag migration in an amorphous solid state electrolyte at elevated temperatures in the presence of a finite electric field. Our model comprises an Ag anode, a GeS_2 electrolyte, and a Pt cathode. The system is complicated, far from homogeneous, and with an elongated cell dimension. To overcome the above issues with the field strength and electronic convergence, we have used an external electrostatic potential with a sawtooth profile. This requires that the model structure include a vacuum layer where the periodic potential returns to its original value. Our DF/MD simulation strategy is similar to that used to study the crystallization of amorphous PCM materials [21,22] and Sb [23], with replications at different temperatures and system sizes that highlight the stochastic nature of the process.

Ag ions do not migrate to the Pt electrode in the presence of an electric field at 380 K in simulations of up to 1 ns, and the process has been accelerated by raising the temperature to between 480 and 680 K, which favors the thermally activated component of Ag diffusion driven by the entropy of mixing. The electronic structure of selected snapshots with percolating Ag networks have been analyzed to clarify the changes in the projected (local) electronic density of states (DOS), effective charges and polarization across the system. The methods of simulation and electronic structure calculations are outlined in Sec. II, and the results are presented in Sec. III and discussed in our concluding remarks (Sec. IV).

II. METHODS

A. Density functional/molecular dynamics simulations

The DF/MD simulations were carried out with the CP2K program package [24], which uses a dual basis set of Gaussian functions and plane waves for the description of electronic structure in conjunction with Goedecker-Teter-Hutter pseudopotentials [25]. The Gaussian basis uses molecularly optimized double-zeta basis functions [24], and the plane waves have a kinetic energy cutoff of 400 Ry for the valence electron density. The valence configurations are $4d^{10}5s$ for Ag, $3s^23p^2$ for Ge, $3s^23p^4$ for S, and $5s^25p^65d^{10}$ for Pt, and we have adopted the exchange-correlation energy functional of Perdew, Burke, and Ernzerhof (PBE) [26]. Periodic boundary conditions have been applied in x, y, and z directions, and a single point (Γ) is used for sampling $\mathbf{k}$ space. The Born-Oppenheimer MD simulations have been carried out using a time step of 3 fs and a canonical sampling through a velocity rescaling thermostat [24]. Short benchmark MD calculations at 480 K for shorter time steps show that the present choice of time step is satisfactory (see Fig. S1 in the Supplemental Material [27]). At each step, the electronic trial density is predicted from the previous values using the stable ASPC algorithm [28]. The production simulation times were 1003 ps (380 K), 503 ps (480 K), and 413 ps (680 K).

The large model (1019 atoms, Fig. 1) comprises an active Ag electrode with a pyramidal tip (342 atoms), an intermediate chalcogenide region of amorphous GeS_2 (138 Ge and 274 S atoms), and a passive Pt electrode (265 atoms) with a truncated tip. The structure of the amorphous chalcogenide region is based on simulations of a bulk sample of 900 atoms obtained from reverse Monte Carlo (RMC) analysis of x-ray diffraction and neutron scattering data [29]. This structure was inserted between the electrodes; overlapping Ge/S atoms were removed while retaining the initial GeS_2 composition. The resulting structure was optimized and thermalized at the target temperature (380, 480, or 680 K) by performing MD simulations (1–2 ps) before starting the production runs. The external electric field of 0.20 eV/Å is represented by a sawtooth potential, and vacuum regions of 5 Å outside both electrodes allow the restoration of the field for periodic images. There is no vacuum in the x and y directions. During MD, the atoms in the outermost layers of the Ag/Pt electrodes

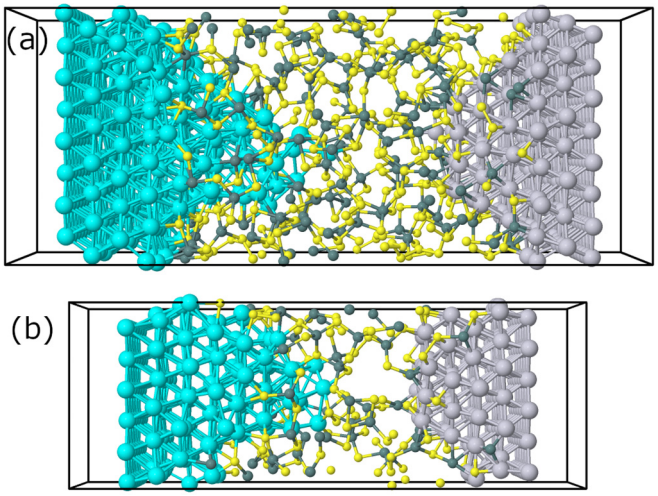

FIG. 1. (a) Starting structure of large model at 480 K (1019 atoms, cell size $22 \times 22 \times 55.5$ Å^3, including a vacuum region of 10 Å outside the electrodes). (b) Starting structure of small model at 420 K (472 atoms, cell size $16.5 \times 16.5 \times 45.5$ Å^3). Ag, cyan; Ge, dark grey; S, yellow; Pt, grey. Structural representations use the Jmol software [30].

(64 atoms each) are fixed to avoid system drift and atoms leaking into the vacuum regions. The initial electrolyte region has a thickness of 34 Å (overlapping the tips), and the minimum distance from the outermost Ag atom to the Pt electrode is 12 Å.

A smaller model was constructed to enable faster simulations at a lower temperature (420 K). The lateral base of the electrodes was reduced from 8×8 atoms (22 Å) to 6×6 (16.5 Å), while the cell size in the perpendicular direction was reduced by 10 Å. One base layer of each electrode was removed and the Ag tip truncated. The resulting system comprised 472 atoms: 192 in the Ag tip, 138 in the chalcogenide region (46 Ge, 92 S), and 144 in the Pt electrode. The outermost layers of Ag and Pt were again fixed, and there was a vacuum region of 10 Å between the repeating units in the z direction. The chalcogenide region was initially 24 Å wide (including the overlapping tips), and the minimum distance between the outermost Ag and Pt electrodes was 10 Å. The same starting structure was used for three simulations of over 500 ps with different initial velocity distributions.

B. Electronic structure analysis

The electronic densities of states (eDOS) of selected snapshots from the 1019-atom trajectories at 480 and 680 K were computed by performing single-point electronic structure calculations using the nonlocal, hybrid PBE0 functional [31]. The computational cost is reduced by using the auxiliary density matrix method, in which the electron density is mapped onto a much sparser Gaussian basis set containing less diffuse and fewer primitive Gaussian functions than otherwise employed [32]. The Bader effective charges for Ag, Ge, S, and Pt atoms were computed from the total electronic charge density [33], and the electrostatic potential and polarization were determined by repeating the calculation with field ON/OFF for fixed snapshots.

III. RESULTS

Ag migration and a percolating metal network across the sample were found at 420 and 480 K, but Ag migration to the Pt electrode did not occur at 380 K within 1 ns. The simulations confirm the tendency of Ag to diffuse readily through the chalcogenide region, while Pt remains largely inert. Ag diffusion is counterbalanced by the movement of Ge and S atoms, where S atoms, in particular, tend to penetrate into the Ag electrode. The percolating Ag network starts from single Ag chains, becomes a branched network of interconnected chains, and small Ag clusters form gradually on the Pt electrode.

A. Dynamics and structure

1. Simulations at 480 and 680 K

The average longitudinal (z direction) displacement of elements is shown for the simulations at 480 and 680 K in Fig. 2, together with the number of Ag atoms connected to the Pt electrode via Ag-Ag and Ag-Pt bonds. The Ag atoms belonging initially to the pyramidal tip are shown in Figs. 2(a) and 2(b). The displacement curves show that mobility in Ag increases significantly more than in Ge and S, which move in the opposite direction. At 480 K, the drifts of Ge and S are very similar and appear to compensate Ag diffusion, while the larger S drift at 680 K reflects its negative effective charge and tendency to bind to Ag. The mobility of atoms in the Ag tip is significantly higher for most of the simulation at 480 K, but ultimately approaches the average Ag value.

In order to gain insight on the forming Ag network on the passive Pt electrode, we have mapped interlinked metal-metal connections, as well as percolation if the network extends from Pt back to the active electrode, by requiring that each Ag-Ag (Pt-Ag) link ("bond") be smaller than a cutoff distance of 3.5 Å. Our choice of this value arises from our previous experience of the Ag-Ag PDF in amorphous chalcogenides [15,16], where there is a minimum at 3.5 Å after the first peak corresponding to nearest neighbors. The subsequent electronic structure analysis suggests that percolation in this context is a topological measure of the Ag distribution across the electrolyte and should not be confused with conductivity changes. The percolation analysis of the simulations at 480 and 680 K is displayed in Figs. 2(c) and 2(d). The tip atoms reach the opposite Pt electrode after 120 ps at 480 K and percolation occurs after 300 ps [Fig. 2(c)]. At 680 K, the first Ag migration occurs after 50 ps, and percolation appears first at 70 ps [Fig. 2(d)]. The accumulation of Ag on the Pt side leads to a lower ionic mobility than in the other Ag atoms. Percolation is occasional at 480 K during the whole simulation, but continuous at 680 K after 300 ps.

Figures 3 and 4 show the trajectories at 480 and 680 K, respectively, with percolating Ag networks highlighted in gold. The results confirm those in Fig. 2, which show outermost Ag (tip atoms) drift towards the Pt side (up to 200 and 100 ps at 480 and 680 K, respectively), until they face the opposing electrode. The first percolating frame at 316 ps is shown for 480 K, where a wire of Ag atoms extends through the chalcogenide to a small Ag cluster on the Pt side. This wire is unstable, however, as shown at 400 ps (all Ag-Ag and Ag-Pt bonds are required to be shorter than 3.5 Å).

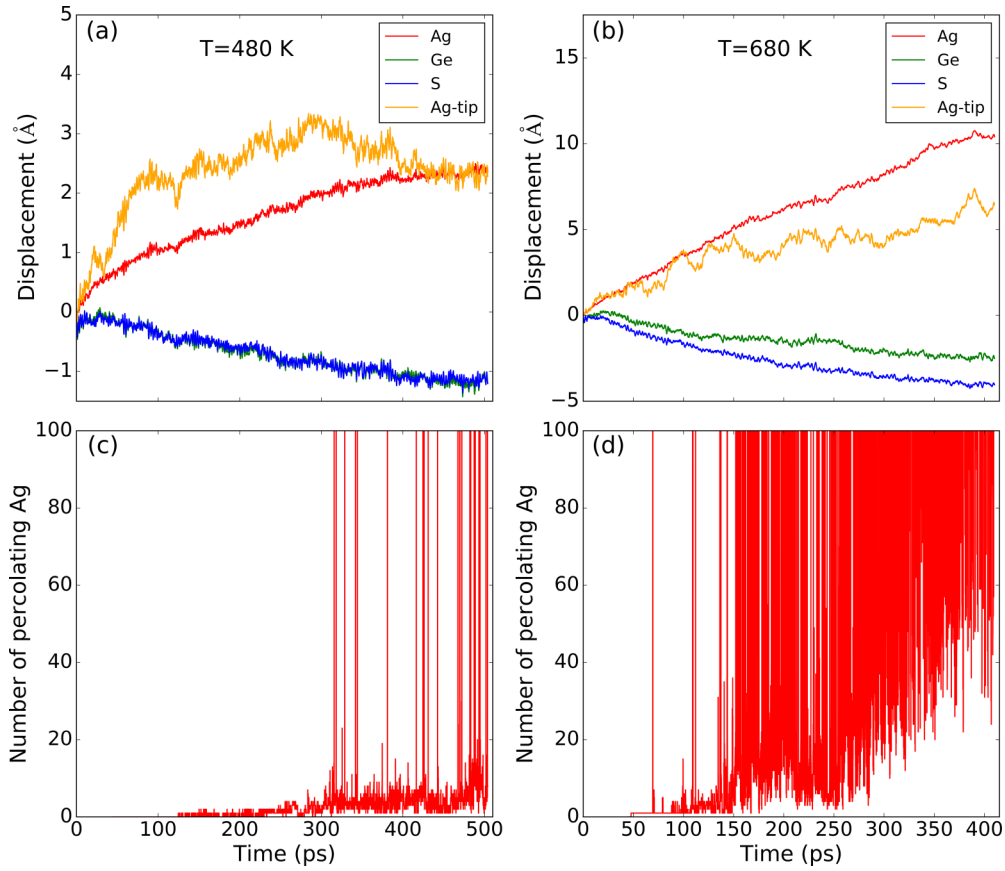

FIG. 2. Average longitudinal displacement of elements and formation of migrated Ag segments/percolating connections from the Pt electrode (nearest neighbor cutoff 3.5 Å). (a),(b) Displacement at 480 and 680 K. (c),(d) Percolation at 480 and 680 K.

Percolation switches on and off during the remainder of the simulation, but Ag migration increases accumulation on the Pt electrode. Another percolating wire is shown at the end of the 480 K simulation (500 ps), where the number of Ag atoms on the Pt side has increased [Fig. 2(c)]. In addition to the percolating network, there are several migrating Ag^+ ions in the chalcogenide region. The Ag tip has dissolved during the simulation, and some Ge and S atoms have penetrated the Ag electrode up to the fourth layer of the initial slab. The Pt electrode remains remarkably intact.

Diffusion is more rapid at 680 K (Fig. 4). The accumulation of Ag ions on the Pt side is fast, and the snapshots at 200 and 400 ps show complex Ag networks with interconnected or branched chains. The Ag electrode is largely dissolved, and most Ag ions are mixed with Ge and S, including Ge/S incorporation up to the second Ag layer. The local coordination of the interfacial Pt atoms has changed, but the Pt electrode is intact. From an energy point of view, the potential energy reduces by 14.2 and 13.6 eV during the MD simulations at 480 and 680 K, respectively, indicating that Ag migration (formation of Ag-S compounds) is energetically favorable. Mixing entropy may reduce the stability of the Ag electrode at the higher temperature, which is near the glass transition temperature of GeS_2 (∼760 K [34]). The results at 680 K must then be assessed with caution, while we expect diffusion at lower T to be more directional, and Ge and S atoms should mix less readily with the Ag electrode.

Figure 5 shows the laterally averaged concentrations of Ag and Pt at the beginning and end of the simulation at 480 K. A corresponding plot for the end structure at 680 K is shown in Fig. S2 in the Supplemental Material [27]. The starting situation (0 ps) is almost identical in the two simulations, with a protruding Ag tip and a solid electrolyte. At the end of the 480 K simulation [Fig. 5(b)], Ag has accumulated on the Pt side, and Ag atoms are present throughout the electrolyte. At 680 K, Ag diffusion is more complete, with a more uniform distribution across the chalcogenide and increased weight on the Pt side. The dissolution of Ag layers is evident. At 680 K, the Ag concentration overlaps with Pt due to the truncated tip structure, where Ag is in contact with the whole Pt surface, but there is no mixing of Ag and Pt.

The GeS_2 electrolyte contains numerous cavities, and their volume in the original bulk GeS_2 structure (900 atoms) is 12.4% (cutoff radius 3.2 Å [35]). The volume depends significantly on the choice of cutoff radius, and the value used for $Ge_{42}S_{58}$ in our previous work (2.5 Å [16]) gives 55.4%. These cavities are occupied by Ag during migration [6] and can host other guest atoms or molecules [36]. We have shown previously that they contribute to Ag diffusion by allowing occasional jumps across vacant sites [16]. Similar observations of cavities acting as "trapping centers" have been made for Ag in GeS_2 [37,38]. Figure 6 shows cavities for the large model at the beginning (0 ps) and the end (500 ps) of the simulation at 480 K. At the end [Fig. 6(b)], there is a visible increase

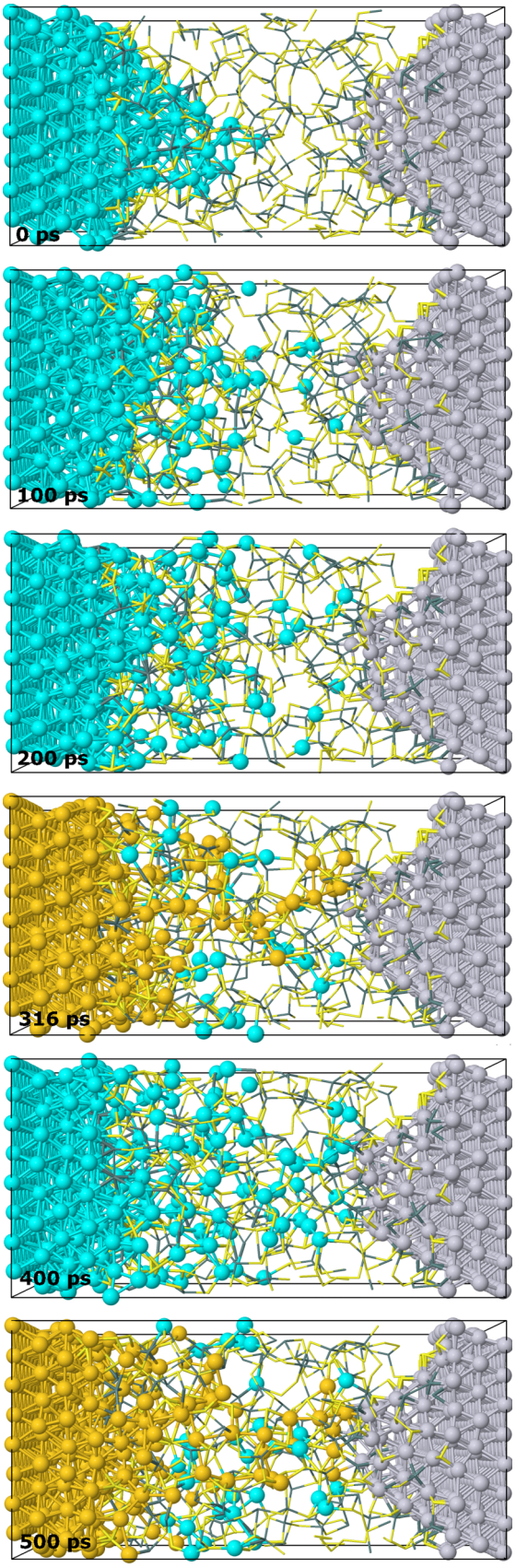

FIG. 3. Simulation at 480 K. Color code: Ag, cyan; percolating Ag, gold; Ge, dark grey; S, yellow; Pt, grey. Ge and S atoms are shown in stick representation for clarity.

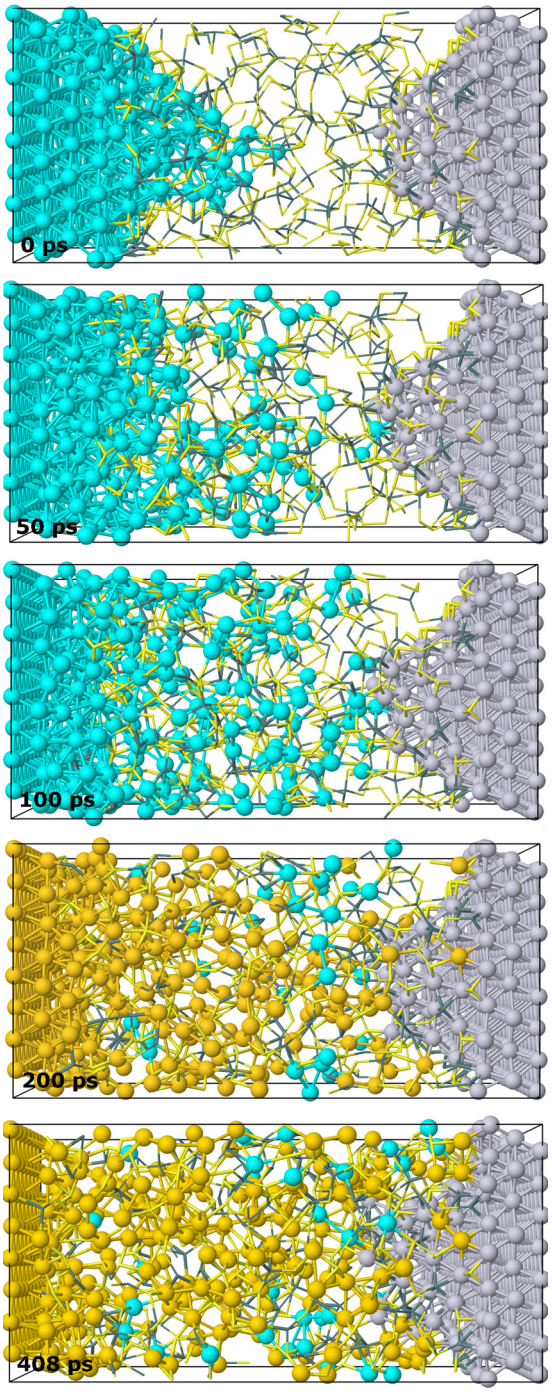

FIG. 4. Simulation at 680 K. Color code and representation of elements as in Fig. 3.

of the cavity volume on the Pt side, while few cavities are evident on the Ag side. There are very few at the center of the cell, where the percolating Ag network has occupied the free volume. This asymmetry correlates with the observed drift of Ge and S towards the Ag electrode. By contrast, the mixing of Ag and the chalcogenide is complete throughout the cell at the end of the 680 K simulation, with only a few small cavities (Fig. S3 [27]).

The analysis of the local coordination of elements in the electrolyte focuses on the arrowed area in Fig. 5. Table I

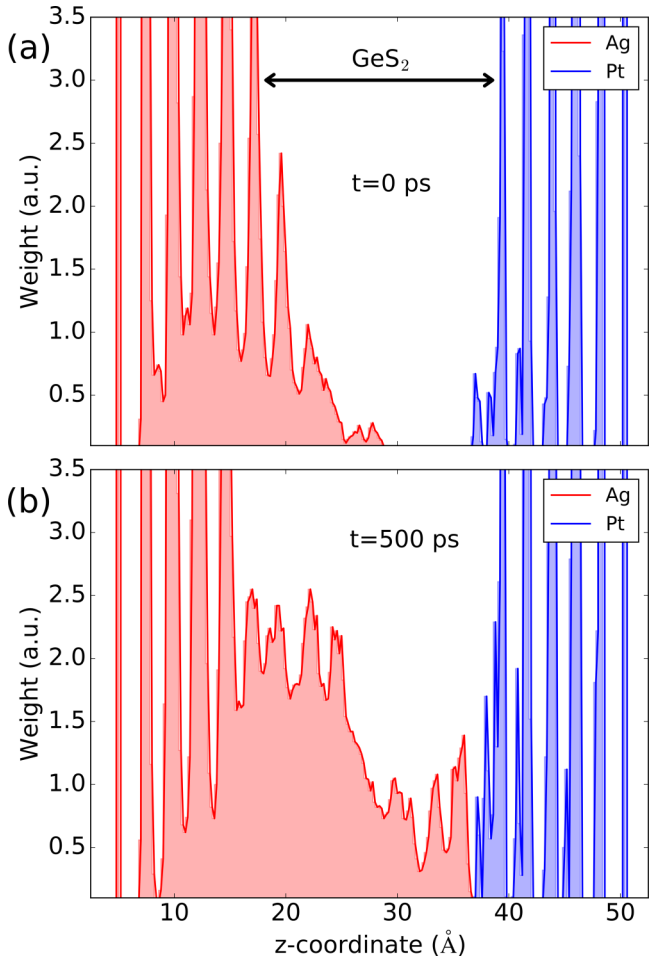

FIG. 5. Local concentration of Ag and Pt as a function of distance. (a) Beginning (0 ps) and (b) end (500 ps) of 480 K simulation averaged over the first (last) 30 ps (50 ps), respectively. The double-headed arrow shows the chalcogenide region (18–40 Å) used for coordination number and bond angle analyses.

shows the total coordination numbers and for pairs of elements at 480 K. Individual cutoff distances are based on the first minimum in the corresponding pair distribution functions (PDF). The starting situation reflects the structure of the Ag tip, where Ag-Ag coordination is large, and the Ag-S coordination indicates that the tip is covered by sulfur. The large Pt-Pt coordination is related to the outermost tip atoms of the passive electrode (included in the analysis), while the tip coverage by Ge and S is of the same magnitude (1.02 and 1.37, respectively). The Ge and S coordination numbers (3.93 and 2.43) are consistent with the bulk GeS_2 structure and the "$8-N$ rule", where N is the number of valence electrons, and corner-sharing Ge tetrahedra dominate [39,40]. The small increase for S coordination is due to bonding to metal atoms.

The Ag tip has dissolved at the end of the simulation (500 ps), and the low Ag-Ag coordination number (1.29) reflects the electrolyte environment and the chainlike structures. Figure 3 shows several isolated Ag atoms. The Ge coordination number changes little, but the S coordination number (3.10) increases significantly due to interaction with Ag. The Ag-S value (3) shows that dissolved Ag atoms bond readily

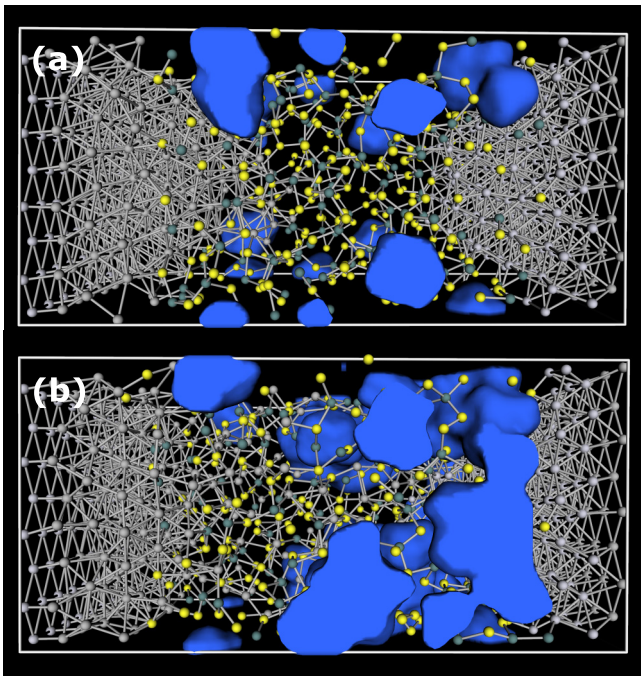

FIG. 6. Cavities at (a) beginning (0 ps) and (b) end (500 ps) of 480 K simulation (cutoff radius 3.2 Å, cavity domains assigned using all atoms [35]). Silver: Ag and Pt atoms.

with S. The overall Pt coordination number is almost unchanged, and the small value for Pt-Ag (0.18) shows that Ag migration is far from complete.

The bond angle distributions for Ag and S are shown in Fig. S4 [27]. The Ag-Ag-Ag distribution at 0 ps reflects the initial Ag tip with an FCC structure with prominent bond angles at 60°, 120°, and 180°. The subsequent Ag migration causes a much flatter distribution between 60° and 180°, with a small maximum at 60° that increases slightly at the end of the simulation (500 ps) as Ag clusters form on the Pt side.

Table II shows the coordination numbers for the simulation at 680 K. The values for the beginning of the simulations are generally consistent with the results at 480 K, although Ag-Ag is reduced at the higher temperature due to rapid dissolution.

TABLE I. Coordination numbers (averaged over 50 ps) in chalcogenide region at beginning and end of the 480 K simulation. The cutoff distances (in Å) are determined from the first minimum of the corresponding PDF: r(Ag-Ag) = 3.5, r(Ag-Ge) = 3.0, r(Ag-S) = 3.2, r(Ag-Pt) = 3.5, r(Ge-Ge) = 3.0, r(Ge-S) = 3.0, r(Ge-Pt) = 3.0, r(S-S) = 2.5, r(S-Pt) = 3.0, and r(Pt-Pt) = 3.5.

Time	Element	Ag	Ge	S	Pt	Sum
0 ps	Ag	5.89	0.29	1.53	0	7.71
	Ge	0.10	0.29	3.36	0.19	3.93
	S	0.27	1.75	0.30	0.12	2.43
	Pt	0	1.02	1.37	6.41	8.80
500 ps	Ag	1.29	0.36	2.96	0.04	4.65
	Ge	0.29	0.17	3.19	0.27	3.92
	S	1.13	1.63	0.21	0.13	3.10
	Pt	0.18	1.27	1.38	6.06	8.89

TABLE II. Coordination numbers (averaged over 50 ps) in chalcogenide region at beginning, middle, and end of 680 K simulation (cutoff distances as in Table I).

Time	Element	Ag	Ge	S	Pt	Sum
0 ps	Ag	4.60	0.26	2.00	0	6.87
	Ge	0.09	0.25	3.37	0.18	3.89
	S	0.34	1.76	0.28	0.11	2.50
	Pt	0	1.08	1.32	6.32	8.72
200 ps	Ag	1.70	0.37	2.80	0.07	4.96
	Ge	0.47	0.20	2.71	0.36	3.74
	S	1.97	1.53	0.04	0.12	3.65
	Pt	0.56	1.71	1.17	5.39	8.84
400 ps	Ag	2.28	0.42	2.58	0.18	5.45
	Ge	0.71	0.22	2.47	0.51	3.90
	S	2.41	1.40	0.01	0.12	3.93
	Pt	1.32	2.21	1.00	3.84	8.36

The results at 200 ps are similar to those at the end of the simulation at lower T, but the migration on the Pt side is more complete. Pt-Ge is larger than Pt-S, which correlates with the increased drift of S towards the Ag electrode [Fig. 2(b)].

Ag accumulation on the Pt side at the end of the simulation (400 ps) leads to increases in the Ag-Ag and Pt-Ag coordination numbers (2.28, 1.32, respectively), and mixing of Ag and chalcogenide has resulted in a further increase in the S-Ag coordination. The Ge-S (S-Ge) coordination decreases from 3.37 (1.76) to 2.47 (1.40) during the simulation, showing that the covalent network is changed by the presence of Ag. The effect is smaller but still evident at 480 K (Table I). The final structure at 680 K shows the greatest similarity to our previous work on bulk $AgAsS_2$ [15] and $Ag_x(Ge_{42}S_{58})_{100-x}$ [16]. In both cases, strong Ag-S bonding resulted in an increase in the coordination number of sulfur (3.6–3.7), while Ag is sixfold coordinated.

2. Simulations at 380 K and 420 K

The final configuration of the 1 ns simulation at 380 K is shown in Fig. S5 [27], and it is clear that the lower temperature has slowed the kinetics significantly. The Ag tip atoms have dissolved, but the sluggish Ag diffusion means that the outermost Ag only reached the center of the electrolyte region. By contrast to higher T (Fig. 2), Ge and S do not show (average) drift towards the Ag electrode, as the tendency to mix Ag is reduced and the covalent network appears to be more rigid.

In order to test the findings for the large model systems, we have performed three parallel simulations (*run*1, *run*2, *run*3, 500 ps each) for the smaller model at a lower temperature (420 K). The starting structure and temperature were the same, but the velocity distributions differed, and all three showed Ag migration to the Pt electrode (onset below 200 ps, see Fig. S6 [27]). The percolation behaviors were, however, very different (see Fig. S7 [27]): *run*1 showed almost continuous percolation between 400 and 500 ps, *run*2 did not percolate at all, and *run*3 showed occasional percolation between 200 and 400 ps that then ceased.

Analysis of individual trajectories (*run*1) of the 10 outermost Ag atoms (tip) shows diverse behavior: Half of the atoms migrate towards Pt, while others interchange with the deeper layers of the Ag electrode, releasing new atoms that diffuse and form percolating networks with the (migrated) atoms from the tip. The interchange is enabled by the lateral component of diffusion and the presence of cavities near the tip interface. A similar behavior was observed for the large model structure at 480 K (Fig. S8 [27]).

TABLE III. Average Bader charges of elements for snapshots of large model structure (field OFF) at time t. Values in parentheses denote standard deviations.

T (K)	t (ps)	Ag	Ge	S	Pt
480	0	0.04 (0.08)	0.10 (0.14)	−0.09 (0.17)	0.01 (0.08)
480	500	0.13 (0.16)	0.09 (0.11)	−0.20 (0.20)	0.01 (0.08)
680	410	0.27 (0.16)	0.10 (0.08)	−0.38 (0.19)	0.01 (0.08)

B. Electronic structure

The electronic structures of selected snapshots during the production MD runs have been recalculated with a hybrid functional (PBE0 [31]) with (ON) and without (OFF) the external electric field. First, we evaluated the effective charges of individual atoms in zero field using the method of Bader [41]. The average values for three snapshots (Table III) show that Ag and Pt are uncharged at the beginning, as expected from the intact electrodes, but the Ag atoms become cationic on entering the chalcogenide region. S atoms gain electrons, especially at 680 K where the mixing is more complete, while the average values of Ge atoms change little. The Pt electrode shows little change, even at 680 K.

Individual effective charges provide a more comprehensive picture of the changes in local electronic structure, and Fig. 7 shows the charges on metal atoms and a scatter plot of individual charges for all atoms at 480 K without the external field. Both electrodes are metallic at the beginning [Figs. 7(a) and 7(c)], and there is an increasingly positive charge on the Ag tip atoms as Ag-Ag coordination decreases. The nearby sulfur atoms bonded to Ag have an enhanced negative character, in contrast to the rest of the chalcogenide region. For Ge and S, there are some outliers (Ge positive, S negative) corresponding to undercoordination with respect to the covalent Ge-S network.

Increased Ag migration after 500 ps [Fig. 7(b)] results in a percolating wire in the center of the supercell with a pyramidal cluster connecting the Pt electrode (Fig. S9 [27]). The effective charges in the middle of the wire are markedly cationic, as for the other dissolved Ag atoms interacting with S, but the charges are reduced again for the Pt-facing cluster. We note that the Ag-Ag bond cutoff (3.5 Å) is considerably larger than the typical Ag-Ag distance in the bulk, and a directional analysis of the electron localization function (values below 0.2, not shown) does not indicate metallic bonding (reference value 0.5) along the single-atom chain. This suggests that accumulation of Ag on the Pt side ("clustering") leads gradually to local metallicity, but this may not be true for single-atom strings in the electrolyte region. The increased Ag-S coordination also results in more sulfur anions, particularly near the Ag electrode.

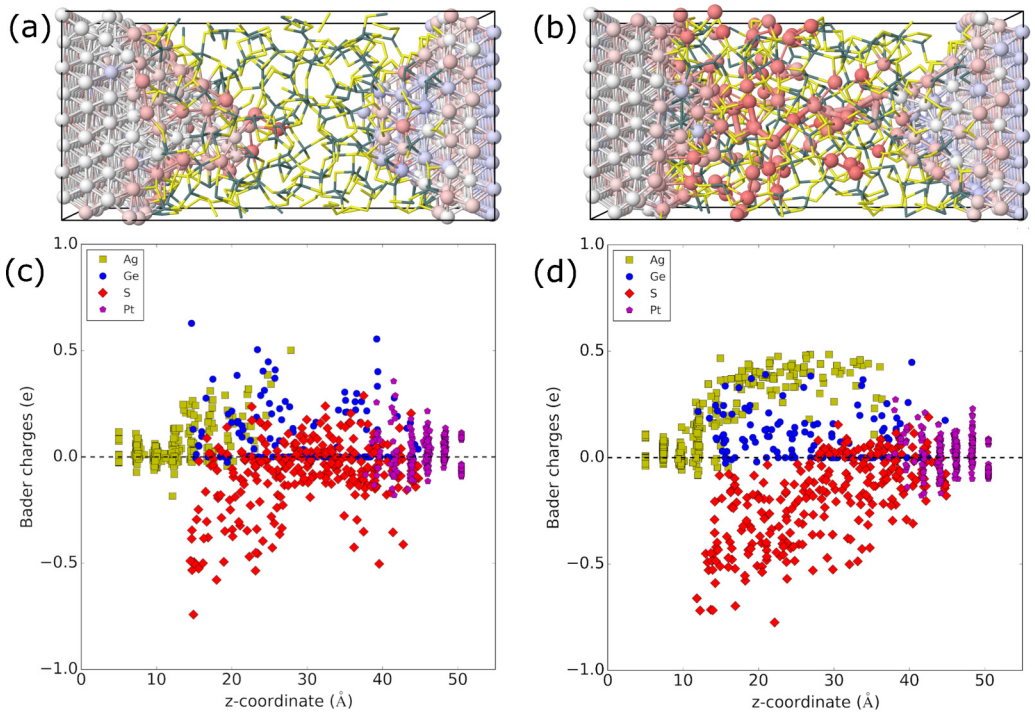

FIG. 7. Effective charges (Bader) for metal atoms (Ag/Pt) and scatter plot of charges for all atoms as a function of location (480 K, field OFF). (a) Starting configuration (0 ps) and (b) snapshot at the end (500 ps). Color scheme: blue (negative) to red (positive), based on effective charge (Ag/Pt). S (yellow) and Ge (dark grey) are shown in stick representation. (c),(d) The corresponding scatter plots.

The strong mixing of Ag with GeS_2 at 680 K leads to Bader charges for sulfur anions with a more homogeneous distribution (Fig. S10 [27]). There are also more Ag cations, as only the two leftmost electrode layers have not dissolved. The enhanced migration of Ag leads to some clusters near the Pt electrode (Fig. S9 [27]). Despite the increased percolation of the Ag network (compared with 480 K), there is no increased tendency for Ag cluster percolation/aggregation on Pt due to strong mixing with S in the electrolyte.

The Bader charge analysis for the selected snapshots with external potential (field ON) reveals only minor changes in individual charges. On average, the values are shifted by $\pm(0.01 - 0.02)e$ / atom for Ag (accumulation) and Pt (depletion), while the effect on Ge and S is an order of magnitude smaller. The effect is most pronounced for the vacuum-facing (fixed) electrode layers. The laterally averaged electrostatic potential of the percolating snapshot at 480 K is shown in Fig. 8 with the electrostatic field ON and OFF, together with the external sawtooth potential. The electrode regions (metal planes) can be clearly identified. The corresponding polarization (Fig. 8, inset) occurs mainly on the vacuum-facing Ag/Pt layers, and there is very little effect inside the electrolyte. The charge transferred between the left and right half cells was -4.28 e, and the initial and final structures at 680 K gave similar values.

The projected densities of states (PDOS) of the initial structure and the percolating snapshot at 480 K are shown in Fig. 9. Most of the metal atoms reside in the electrodes, so that the DOS has major contributions from Ag-4d and Pt-5d components below -10 eV, and the system is metallic in the lateral direction. The Ag-PDOS profile reveals interesting details: The shoulder at -6.5 eV is reduced as a result of migration while the peak at -4.5 eV is enhanced. There is increased weight in the plateau starting at -3.5 eV, while the weight

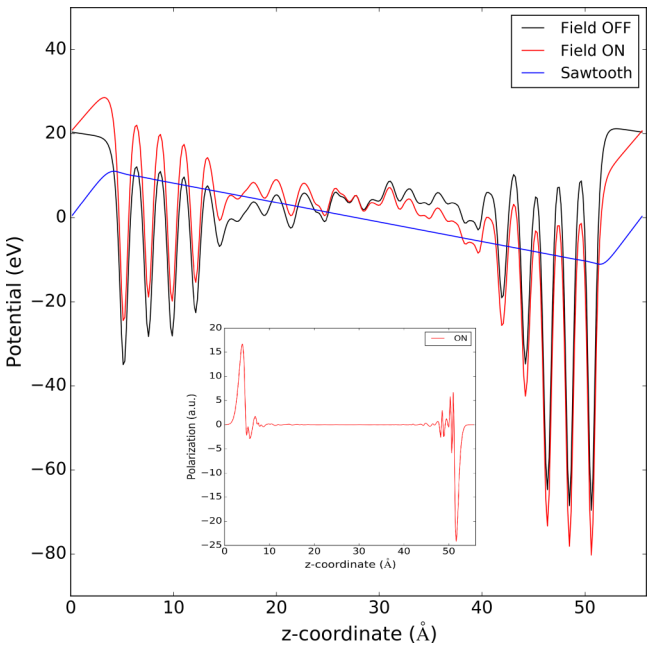

FIG. 8. Laterally averaged electrostatic potential and polarization (inset) as a function of location for a snapshot at the end (500 ps) of the 480 K simulation. The electrostatic potential is calculated with the field ON/OFF (-0.20 eV/Å). Blue: external sawtooth potential. Polarization dominates in the vacuum-facing layers and the charge transferred is 4.28e (electron accumulation on Ag side).

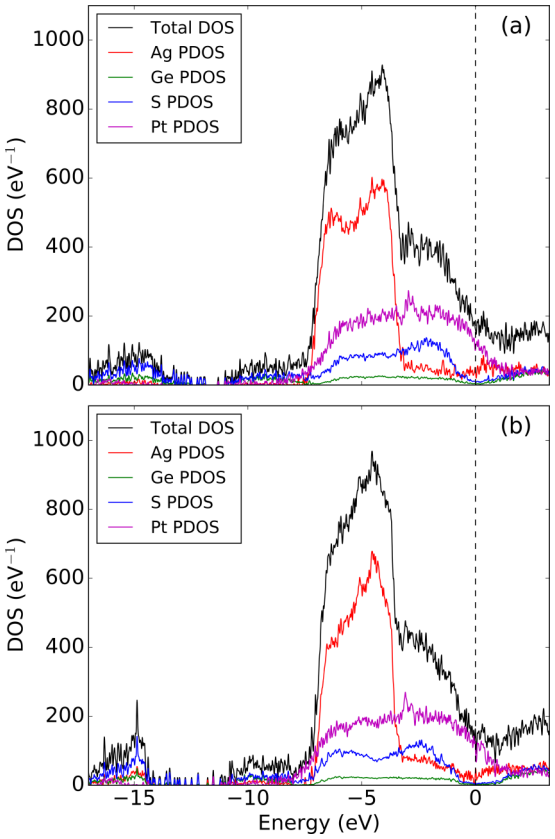

FIG. 9. Electronic density of states (DOS) and projections onto elements for 480 K simulation (field OFF). (a) Starting configuration (0 ps) and (b) snapshot at the end (500 ps) of simulation.

at Fermi level decreases. This modulation of Ag-PDOS is even more pronounced at 680 K (Fig. S11 [27]), where the main peak becomes stronger, the plateau becomes a shoulder, and the weight at the Fermi level falls to zero. The PDOS of Ag is very similar to those found in our previous studies of amorphous $Ag_{20}(Ge_{42}S_{52})_{80}$ and $AgAsS_2$ [15,16]. The S-3p component shows the evolution of a local maximum deeper in the valence band around −6.5 eV. This effect is greater for the final structure at 680 K, where the mixing with Ag is enhanced. The small changes in Ge-PDOS are consistent with the calculated Bader charges.

The metallic electrodes contribute in a major way to the total DOS, while the electrolyte region is crucial for electronic transport. To gain insight into possible changes in conductivity, we have calculated the local density of states (LDOS, Fig. 10) in a slice of 10 Å thickness at the center of the electrolyte region of the percolating snapshot. There is zero weight in the band gap of ∼2 eV, which confirms that the finite weight of DOS is due solely to the electrodes, particularly Pt. The PDOS for the percolating Ag string across the electrolyte in the same snapshot shows some weight across the band gap, and the LDOS of the slice has contributions from Ag atoms at the center of the wire. By contrast, the finite weight of the wire PDOS at Fermi level is caused by the string ends, and there is no contribution from the center of the wire. This indicates that conduction across the single-atom Ag wire is unlikely.

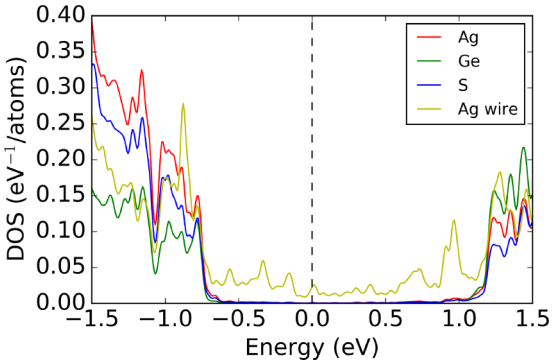

FIG. 10. Local DOS (field OFF) around the Fermi energy for a 10 Å slab at center of electrolyte region compared with the percolating Ag wire for the snapshot at 500 ps [Fig. 7(b)].

IV. DISCUSSION AND CONCLUDING REMARKS

We have simulated the migration and accumulation of Ag cations in a model of a real CBRAM cell with a solid-state electrolyte and active/passive metallic electrodes in the presence of a finite electric field. The DF/MD approach is applied to amorphous GeS_2 sandwiched between Ag and Pt electrodes and provides unique information about the atomic structure, dynamics and electronic structure for each time step. The high computational expense limits the accessible time scales to around 1 ns, and we have repeated the Ag migration simulations at several temperatures to clarify the physical processes involved. We provide information on the formation of metallic filaments in CBRAM cells, and we believe that these are the first such simulations using DF energies and forces throughout.

The dynamics of Ag are sluggish at 380 K, with occasional jumps across cavities ("trapping centers"), and no Ag reaches the Pt electrode during a 1 ns simulation. Simulations at 420 K (small model) and 480 K (large model) show Ag migration and percolating Ag wires through the GeS_2 electrolyte, but the percolating connections are not yet stable after 500 ps. At 680 K, most of the Ag electrode has dissolved, and rapid Ag diffusion is driven by free energy (formation energy, mixing entropy). Ag reaches the Pt electrode rapidly, after which percolation becomes continuous. The high temperature results in a rather homogeneous Ag/electrolyte region, and the local coordination resembles that of the bulk Ag/Ge/S glass [16]. The passive Pt electrode is remarkably stable, even at 680 K.

The data from the 480 K simulation (large model) are particularly relevant for CBRAM cell operation and show that the migration of individual Ag atoms has several facets. Not all atoms from the protruding Ag tip reach the Pt electrode, but some penetrate deeper into the active electrode and promote the release of other Ag cations into the electrolyte. Ag migration results in stringlike Ag segments that occasionally form a percolating network across the sample. Increased accumulation of Ag on the Pt side leads to clustering, and a pyramidal Ag cluster that is part of the percolating wire is highlighted in Fig. 7(b). The picture of clustering on the passive electrode is similar to that suggested by Ducry *et al.* [4]. The 680 K simulation occasionally shows small Ag clusters, but their aggregation to larger units is hindered by the high

temperature. Such clustering has been reported to be energetically favorable for Cu in a-SiO_2 at DF level [42], while classical MD simulation have revealed a similar tendency for Ag in Ge/S glasses [43].

The electronic structure analysis (Bader charges, DOS) suggests that clustering is crucial for increased conductivity of metallic filaments, since single-atom Ag wires are not metallic; both the DOS weight at the Fermi energy and the polarization show no sign of increased conductivity. Increased Ag-Ag (and Ag-Pt) coordination on the Pt electrode reduces Ag^+ cations to Ag atoms. Our results indicate that Ag accumulation leads to the formation and fusion of Ag clusters that subsequently form a metallic filament towards the active electrode. Prasai *et al.* [44] have used a special DFT band-gap sculpting technique to modify the atomic structure of a $GeSe_3$:Ag glass and tune the conductivity, leading to a metallic Ag-rich phase (Ag_2Se) and depletion of covalent tetrahedrally bonded $Ge(Se_{(1/2)})_4$ configurations.

S and Ge mix with the active electrode during Ag migration towards Pt, even penetrating into deeper layers at 480 K. Previous experimental work has reported formation of an interface layer upon Ag deposition on GeS_2 [45], and the ReaxFF simulations revealed a CuS_x phase at the active electrode interface [46]. The coordination numbers show that the covalent Ge-S network is affected little by the presence of Ag, indicating a rather rigid electrolyte at low temperatures. Upon migration, the increasing Ag-S coordination results in Ag becoming strongly cationic and S anionic. This effect is strongest at the active electrode interface and weaker on the Pt-side of the electrolyte as Ag accumulates. The atoms with the largest absolute value of effective charge are the most sensitive to the external field, as evident in the drift profiles of the Ag tip atoms at 480 K [Fig. 2(a)] and sulfur at higher T [680 K, Fig. 2(b)]. The weakest link of the metallic filaments in CBRAM cells appears to be the active electrode interface. The SET/RESET phenomenon will be studied by switching the field direction in planned DF/MD simulations of "model filaments" comprising Ag clusters.

Our DF/MD approach has obvious limitations, since the explicit treatment of 10728 valence electrons during MD restricts both system size and time scales. Our model structure of 1019 atoms has sufficient lateral dimensions (22×22 Å^2), but the perpendicular dimension is limited, since the closest distance between the tips is initially 12 Å. A thicker electrolyte region (here 34 Å) will be needed for planned NEGF simulations. Preliminary tests of selected snapshots from the present work showed that the relevant transmission coefficients at the Fermi energy are affected mainly by metal-induced gap states, and a wider chalcogenide region is needed to suppress this effect [47].

Another concern is the applied electric field (0.20 eV/Å) and range of temperatures ($380 - 680$ K) chosen to accelerate the simulations. Although the field is high, its modest effect on electronic structure is shown by small changes in individual effective charges and polarization, and the overall charge transfer of $4.28e$ between the electrodes. Nevertheless, we can extrapolate our findings of atomic motion in a range of (elevated) temperatures to normal operating conditions (300 K). Improved atomistic simulations will require larger atomic models at lower temperatures, and correspondingly longer times. Classical force fields with neural networks may enable significant improvements of these aspects, provided that their accuracy and transferability are satisfactory.

ACKNOWLEDGMENTS

We thank E. Bychkov for providing the RMC structure for amorphous GeS_2 and J. Liu for NEGF simulations of selected snapshots. J.A. and K.K. were supported by the Academy of Finland (Project No. 322832 "NANOIONICS"). Computer time provided by the JARA-HPC Vergabegremium on the JARA-HPC partition of the Jureca supercomputer (Forschungszentrum Jülich) is gratefully acknowledged.

[1] G. W. Burr, M. J. Breitwisch, M. Franceschini, D. Garetto, K. Gopalakrishnan, B. Jackson, B. Kurdi, C. Lam, L. A. Lastras, A. Padilla, B. Rajendran, S. Raoux, and R. S. Shenoy, J. Vac. Sci. Technol. B **28**, 223 (2010).

[2] R. Waser, R. Dittmann, G. Staikov, and K. Szot, Adv. Mater. **21**, 2632 (2009).

[3] H.-Y. Chen, S. Brivio, C.-C. Chang, J. Frascaroli, T.-H. Hou, B. Hudec, M. Liu, H. Lv, G. Molas, J. Sohn, S. Spiga, V. M. Teja, E. Vianello, and H.-S. P. Wong, J. Electroceram. **39**, 21 (2017).

[4] F. Ducry, J. Aeschlimann, and M. Luisier, Nanoscale Adv. **2**, 2648 (2020).

[5] M. L. Urquiza, M. M. Islam, A. C. T. van Duin, X. Cartoixà, and A. Strachan, ACS Nano **15**, 12945 (2021).

[6] I. Valov, R. Waser, J. R. Jameson, and M. N. Kozicki, Nanotechnology **22**, 254003 (2011).

[7] J. Orava, M. N. Kozicki, S. N. Yannopoulos, and A. L. Greer, AIP Adv. **5**, 077134 (2015).

[8] N. Onofrio, D. Guzman, and A. Strachan, Nat. Mater. **14**, 440 (2015).

[9] W. Chen, S. Tappertzhofen, H. J. Barnaby, and M. N. Kozicki, J. Electroceram. **39**, 109 (2017).

[10] E. Covi, W. Wang, Y.-H. Lin, M. Farronato, E. Ambrosi, and D. Ielmini, IEEE T. Electron Dev. **68**, 4335 (2021).

[11] W. Wang, E. Covi, Y.-H. Lin, E. Ambrosi, A. Milozzi, C. Sbandati, M. Farronato, and D. Ielmini, IEEE T. Electron Dev. **68**, 4342 (2021).

[12] S. Ambrogio, B. Magyari-Köpe, N. Onofrio, M. Mahbubul Islam, D. Duncan, Y. Nishi, and A. Strachan, J. Electroceram. **39**, 39 (2017).

[13] W. Li, Y. Ando, E. Minamitani, and S. Watanabe, J. Chem. Phys. **147**, 214106 (2017).

[14] R. O. Jones, Rev. Mod. Phys. **87**, 897 (2015).

[15] J. Akola, P. Jóvári, I. Kaban, I. Voleská, J. Kolář, T. Wágner, and R. O. Jones, Phys. Rev. B **89**, 064202 (2014).

[16] J. Akola, B. Beuneu, R. O. Jones, P. Jóvári, I. Kaban, J. Kolář, I. Voleská, and T. Wágner, J. Phys.: Condens. Matter **27**, 485304 (2015).

[17] L. V. Keldysh, Sov. Phys. JETP **20**, 1018 (1965) [J. Exp. Theor. Phys. **47**, 1515 (1964)].

[18] I. Souza, J. Íñiguez, and D. Vanderbilt, Phys. Rev. Lett. **89**, 117602 (2002).
[19] P. Umari and A. Pasquarello, Phys. Rev. Lett. **89**, 157602 (2002).
[20] K. Konstantinou, F. C. Mocanu, J. Akola, and S. R. Elliott, Acta Mater **223**, 117465 (2022).
[21] J. Kalikka, J. Akola, and R. O. Jones, Phys. Rev. B **90**, 184109 (2014).
[22] J. Kalikka, J. Akola, and R. O. Jones, Phys. Rev. B **94**, 134105 (2016).
[23] M. Ropo, J. Akola, and R. O. Jones, Phys. Rev. B **96**, 184102 (2017).
[24] T. D. Kühne, M. Iannuzzi, M. Del Ben, V. V. Rybkin, P. Seewald, F. Stein, T. Laino, R. Z. Khaliullin, O. Schütt, F. Schiffmann, D. Golze, J. Wilhelm, S. Chulkov, M. H. Bani-Hashemian, V. Weber, U. Borštnik, M. Taillefumier, A. S. Jakobovits, A. Lazzaro, H. Pabst, T. Müller, R. Schade, M. Guidon, S. Andermatt, N. Holmberg, G. K. Schenter, A. Hehn, A. Bussy, F. Belleflamme, G. Tabacchi, A. Glöß, M. Lass, I. Bethune, C. J. Mundy, C. Plessl, M. Watkins, J. VandeVondele, M. Krack, and J. Hutter, J. Chem. Phys. **152**, 194103 (2020), and references therein.
[25] S. Goedecker, M. Teter, and J. Hutter, Phys. Rev. B **54**, 1703 (1996).
[26] J. P. Perdew, K. Burke, and M. Ernzerhof, Phys. Rev. Lett. **77**, 3865 (1996).
[27] See Supplemental Material at http://link.aps.org/supplemental/10.1103/PhysRevMaterials.6.035001 for 11 figures providing additional details of the results.
[28] J. Kolafa, J. Comput. Chem. **25**, 335 (2004).
[29] A. Bytchkov, G. J. Cuello, S. Kohara, C. J. Benmore, D. L. Price, and E. Bychkov, Phys. Chem. Chem. Phys. **15**, 8487 (2013).
[30] Jmol: an open-source Java viewer for chemical structures in 3D. www.jmol.org.
[31] J. P. Perdew, M. Ernzerhof, and K. Burke, J. Chem. Phys. **105**, 9982 (1996).
[32] M. Guidon, J. Hutter, and J. VandeVondele, J. Chem. Theory Comput. **6**, 2348 (2010).
[33] G. Henkelman, A. Arnaldsson, and H. Jónsson, Comput. Mater. Sci. **36**, 354 (2006).
[34] I. Petri and P. Salmon, J. Non-Cryst. Solids **293-295**, 169 (2001).
[35] I. Heimbach, F. Rhiem, F. Beule, D. Knodt, J. Heinen, and R. O. Jones, J. Comput. Chem. **38**, 389 (2017).
[36] G. Ori, C. Massobrio, A. Pradel, M. Ribes, and B. Coasne, Phys. Chem. Chem. Phys. **18**, 13449 (2016).
[37] D. N. Tafen, D. A. Drabold, and M. Mitkova, Phys. Status Solidi R **242**, R55 (2005).
[38] B. Prasai and D. A. Drabold, Phys. Rev. B **83**, 094202 (2011).
[39] S. Blaineau, P. Jund, and D. A. Drabold, Phys. Rev. B **67**, 094204 (2003).
[40] S. L. Roux and P. Jund, J. Phys.: Condens. Matter **19**, 196102 (2007).
[41] R. F. W. Bader, *Atoms in Molecules - A Quantum Theory* (Oxford University Press, Oxford, 1990).
[42] D. M. Guzman, N. Onofrio, and A. Strachan, J. Appl. Phys. **121**, 055703 (2017).
[43] H. Iyetomi, P. Vashishta, and R. K. Kalia, J. Non-Cryst. Solids **262**, 135 (2000).
[44] K. Prasai, G. Chen, and D. A. Drabold, Phys. Rev. Materials **1**, 015603 (2017).
[45] J. H. Horton, K. L. Peat, and R. M. Lambert, J. Phys.: Condens. Matter **5**, 9037 (1993).
[46] N. Onofrio and T. W. Ko, J. Phys. Chem. C **123**, 9486 (2019).
[47] J. Liu and M. P. Anantram, J. Appl. Phys. **113**, 063711 (2013).